



Cite this: DOI: 10.1039/c7ee01764b

Efficient solar-driven electrochemical CO₂ reduction to hydrocarbons and oxygenates†

Gurudayal,^{id abc} James Bullock,^{de} Dávid F. Srankó,^{id af} Clarissa M. Towle,^{id ce} Yanwei Lum,^{id ace} Mark Hettick,^{id de} M. C. Scott,^{cg} Ali Javey^{id de} and Joel Ager^{id *abce}

Received 24th June 2017,
Accepted 31st August 2017

DOI: 10.1039/c7ee01764b

rsc.li/ees

Solar to chemical energy conversion could provide an alternative to mankind's unsustainable use of fossil fuels. One promising approach is the electrochemical reduction of CO₂ into chemical products, in particular hydrocarbons and oxygenates which are formed by multi-electron transfer reactions. Here, a nanostructured Cu–Ag bimetallic cathode is utilized to selectively and efficiently facilitate these reactions. When operated in an electrolysis cell, the cathode provides a constant energetic efficiency for hydrocarbon and oxygenate production. As a result, when coupled to Si photovoltaic cells, solar conversion efficiencies of 3–4% to the target products are achieved for 0.35 to 1 Sun illumination. Use of a four-terminal III–V/Si tandem solar cell configuration yields a conversion efficiency to hydrocarbons and oxygenates exceeding 5% at 1 Sun illumination. This study provides a clear framework for the future advancement of efficient solar-driven CO₂ reduction devices.

Broader context

The continuing rise in Earth's atmospheric CO₂ levels, which is primarily due to anthropogenic combustion of fossil fuels, may be mankind's most enduring legacy on the planet. A number of technologies would need to be developed to reverse this trend. Among them, the conversion of CO₂ to fuels and chemicals using sustainable power sources, analogous to but more efficient than photosynthesis, could directly reduce the rate of CO₂ emission into the atmosphere and as such is a key component of any strategy to stabilize the Earth's atmospheric CO₂ concentration. Reported here is a solar-driven CO₂ reduction system which generates hydrocarbon and oxygenate products with an efficiency far higher than natural photosynthesis, and which also operates capably over the course of a solar day.

Introduction

The development of sustainable energy sources is critical for continued human progress amid rising populations and climbing energy demand. The direct conversion of the abundant solar resource into chemical energy is an attractive approach to meet this challenge.^{1,2} The coupling of photovoltaic (PV) and electrochemical (EC) components provides a means to convert solar energy into fuels and chemicals.^{3,4} While solar-assisted water splitting has been widely studied for hydrogen production,^{3,5,6} there are comparatively few reports of solar-driven electrochemical CO₂ reduction to carbon-containing products.^{3,7–9} Notably, prior to 2015, reported overall conversion efficiencies for solar driven CO₂ reduction did not exceed 1%.³

Recently, a number of devices which perform solar-driven CO₂ reduction have been reported.^{9–12} Arai *et al.* reported an integrated device based on a triple-junction amorphous Si cell with a semitransparent IrO_x anode and polymeric Ru cathode which produced formate with a 4.5% overall energy conversion

^a Joint Center for Artificial Photosynthesis, Lawrence Berkeley National Laboratory, 1 Cyclotron Road, Berkeley, CA 94720, USA. E-mail: jwager@lbl.gov

^b Chemical Sciences Division, Lawrence Berkeley National Laboratory, 1 Cyclotron Road, Berkeley, CA 94720, USA

^c Department of Materials Science and Engineering, University of California Berkeley, Berkeley, CA 94720, USA

^d Department of Electrical Engineering and Computer Science, University of California Berkeley, Berkeley, CA 94720, USA

^e Materials Sciences Division, Lawrence Berkeley National Laboratory, 1 Cyclotron Road, Berkeley, CA 94720, USA

^f Hungarian Academy of Sciences Centre for Energy Research, Surface Chemistry and Catalysis Department, Konkoly-Thege Miklós út 29-33, H-1121 Budapest, Hungary

^g National Center for Electron Microscopy, Molecular Foundry, Lawrence Berkeley National Laboratory, Berkeley, CA 94720, USA

† Electronic supplementary information (ESI) available: Methods, calculation of standard potentials, device efficiency calculations, SEM-EDX, XRD and XPS analysis, ICP-MS analysis, *in situ* Raman spectroscopy, HR-TEM, stability analysis, supplementary electrochemical data, optimization data, techno-economic analysis. See DOI: 10.1039/c7ee01764b

efficiency.⁸ Schreier *et al.* used three series-connected halide perovskite solar cells in combination with an electrochemical cell containing an Au cathode and an IrO₂ anode to produce carbon monoxide with a conversion efficiency of 6.5%.⁷ Zhou *et al.* coupled a TiO₂-protected III-V photoanode, a Pd/C cathode, and a bipolar membrane to achieve a solar-to-formate conversion efficiency of 10%.⁹ Very recently, Schreier *et al.* coupled a GaInP/GaInAs/Ge tandem solar cell to a cell equipped with a bipolar membrane to produce CO at a 1 Sun efficiency of 13.4%.¹²

While these reports are encouraging, achieving solar-driven CO₂ reduction reaction (CO₂ RR) efficiencies comparable to those obtained for water splitting in similar devices (~8–20%),^{5,13,14} two-electron reduction products such as CO and formate would require further processing to be used as fuels. Thus, solar-driven conversion of CO₂ to more highly-reduced products such as hydrocarbons (*e.g.* methane, ethylene) and oxygenates (*e.g.* ethanol) with comparable efficiency remains an unmet challenge. Fig. 1 depicts the components required for a complete solar-driven EC CO₂ reduction device, with an emphasis on the overall voltage requirement. Efficient operation requires the following: (i) a highly active and stable cathode for CO₂ reduction to the desired products; (ii) a durable anode with a low overpotential for the O₂ evolution reaction; (iii) optimization of the cell and

electrolyte for efficient mass transport of the reactants and minimization of resistive losses; (iv) a membrane or other method to allow ion transport and minimize back reactions of the products.

In this work, we selected and optimized each component of the PV-EC system depicted in Fig. 1 with an emphasis on minimizing the voltage losses and on producing hydrocarbon and oxygenate products. With respect to the cathode, which performs the CO₂RR, nanostructured “oxide-derived” (OD) copper electrocatalysts have been demonstrated to increase selectivity to C–C coupled products such as ethylene and ethanol which are the targets of this study.^{15–19} However, OD copper has a relatively small potential window for optimal generation of these products.¹⁵ Instead, we developed a CuAg bimetallic cathode which is active over a wide operational window while maintaining selectivity for C₂ and C₃ products. A CsHCO₃ electrolyte was used, as it has been shown to enhance selectivity to C₂ products compared to KHCO₃,^{20–22} which is more typically employed. To reduce the overall voltage requirement of the cell, we employed an IrO₂ nanotube anode has a very low overpotential for water oxidation neutral-pH electrolyte. These components are combined in a sandwich-type electrochemical cell which has a short cathode-to-anode distance, an anion-conducting membrane, and an efficient gas-to-liquid mass transfer for the CO₂ reactant.^{23,24}

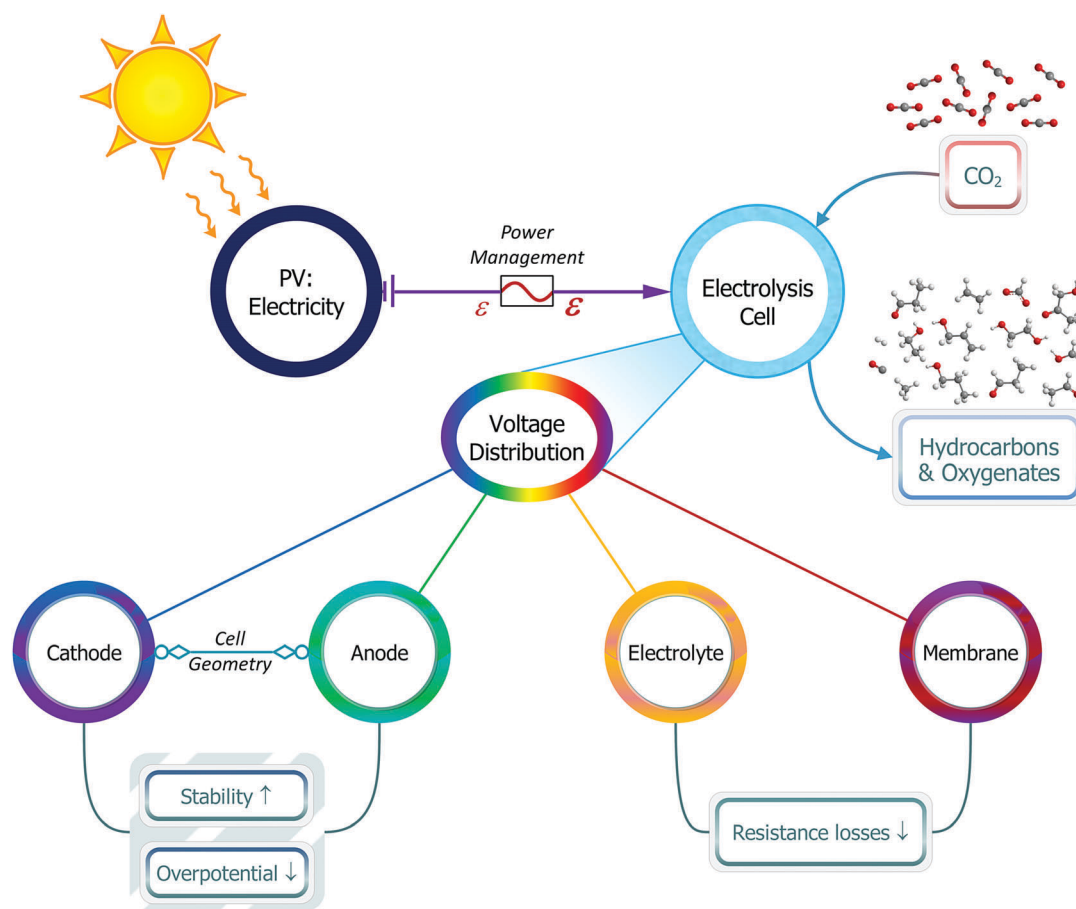


Fig. 1 Components in a prospective system to use renewable solar light to convert CO₂ into chemical products *via* electrochemical reduction. Overpotentials at the cathode and anode and resistive losses in the electrolyte and through the cation/anion conducting membrane (if present) must be minimized in order to achieve a high overall energy conversion efficiency.

We investigated in detail the effect of the electrolyte concentration on the cell current and the resultant product distribution to find optimal values. The power-matching electronics coupling the PV and EC components were selected to achieve high overall efficiency under the varying illumination conditions (0.35 to 1 Sun) which occur over the course of a solar day due to Sun angle and cloud shading. We also developed a power-matching strategy to couple a high-efficiency 4-terminal PV device to the EC cell, and it with this configuration that our highest solar-to-hydrocarbon and oxygenate efficiency is achieved, 5.6%.

Results and discussion

Nanocoral bimetallic cathode with wide window of efficient CO₂RR operation

A selective and active cathode is essential for the efficient operation of the overall device. Although an oxide-derived Cu catalyst was also evaluated in this study (see ESI† for electrochemical data), we found that a Cu-rich nanostructured bimetallic CuAg catalyst is better suited for our overall operating conditions. It provides superior selectivity and current density over the range of voltages expected for variable solar illumination and under the electrolyte conditions required to reduce resistive losses in the cell. A false-color EDX SEM image of this cathode is shown in Fig. 2a and reveals a “nanocoral” morphology formed by dendrites

50–100 nm in length (see also Fig. S1 and S2, ESI†). XPS analysis shows that Ag is present at about 1% atomic concentration and XRD analysis indicates that both metals are polycrystalline (Table S1 and Fig. S3–S5, ESI†). The HRTEM measurements and corresponding HAADF-STEM-EDS mapping of CuAg cathode clearly shows the distribution of copper and silver (Fig. S7 and S8, ESI†).

We performed extensive measurements on the CuAg cathode in the three-electrode geometry to benchmark its performance. Fig. 2b shows the effect of electrolyte concentration (0.1–0.5 M CsHCO₃) on the current density. The current density increases with increasing electrolyte concentration, and the potential required to operate at our target current density of 10 mA cm⁻² is reduced by 170 mV over this range. A higher electrolyte concentration results in a drop in resistive losses across the cell; however, an electrolyte concentration higher than 0.5 M diminishes the C₂–C₃ product selectivity (see ESI† for optimization discussion). A typical product distribution is shown in Fig. 2c for a cathode potential of –1 V vs. RHE (see also Fig. S13b, ESI†). The CuAg cathode shows excellent activity with respect to CO₂ reduction to hydrocarbons and oxygenates and shows only a 30–35% Faradaic efficiency (FE) of hydrogen generation (Fig. 2c), which is less than OD copper at this potential (Fig. S13b, ESI†). The CuAg cathode shows a high faradaic efficiency for ethylene, ethanol, and propanol formation, which is substantially higher than for the oxide-derived catalyst (Fig. 2c and Fig. S13b, ESI†) at the same conditions. We performed a stability assessment for three days

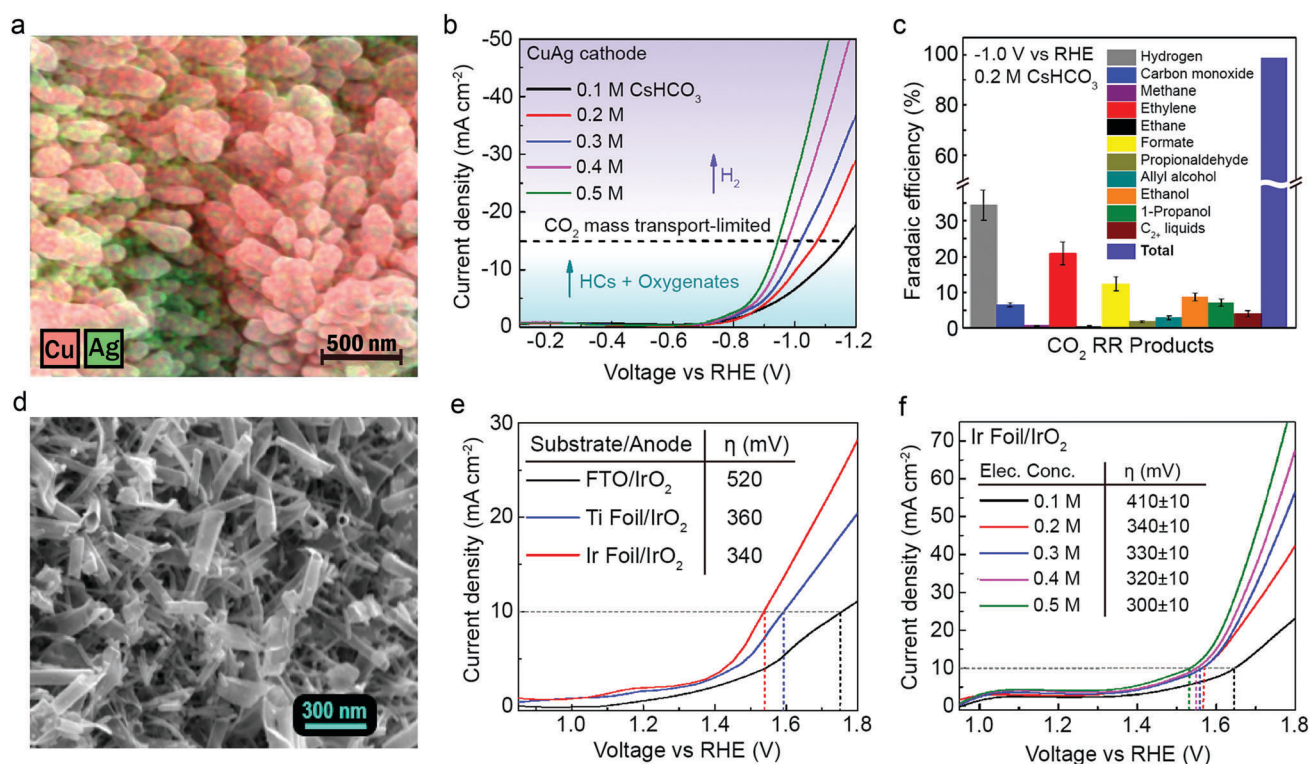


Fig. 2 Structural and electrochemical properties of CuAg cathode and IrO₂ nanotube anode. (a) EDX elemental mapping of CuAg nanocoral cathode. (b) *J*–*V* curves of CuAg nanocoral cathode under various electrolyte conditions. (c) CO₂ RR product distribution at –1 V vs. RHE (~10 mA cm⁻²) in 0.2 M CsHCO₃ electrolyte. Error bars are standard deviations based on replicate experiments. (d) SEM surface view of IrO₂ nanotubes on iridium foil. (e) *J*–*V* curves of IrO₂ nanotube anode on FTO, Ti foil and Ir foil substrates in 0.2 M CsHCO₃ electrolyte. (f) *J*–*V* curve of Ir foil-IrO₂ anode under various electrolyte conditions. Electrochemical measurements were performed under constant CO₂ bubbling (the condition used in the electrolysis cell).

in 0.1 M CsHCO₃ at -1 V vs. RHE and found that the current density and product selectivity were generally stable over this period (Fig. S11, ESI†).

Anode with low overpotential in neutral pH

Selection of an anode material which produces the lowest possible overpotential for the oxygen evolution reaction (OER) is crucial for achieving an overall efficient device. The anode must be stable and operate at near-neutral pH (6.8–7.6) for the range of electrolyte concentrations used here. To this end, we modified a templated electrodeposition procedure for nanostructured IrO₂.²⁵ Notable modifications include the use of hydrothermal growth to make the sacrificial ZnO nanotube template, allowing for deposition on arbitrary substrates, and the use of different electrodeposition conditions (see Methods). As a result, IrO₂ nanotubes with a high surface area morphology are produced as shown in Fig. 2d. Energy dispersive X-ray spectroscopy (EDX) line scan measurements indicate uniform distribution of iridium and oxygen, with no observation of Zn from the template (Fig. S10, ESI†).

Fig. 2e shows the three-electrode J - V curves for IrO₂ nanotubes grown on FTO, Ti, and Ir. The lowest overpotential at our target current density of 10 mA cm⁻², 340 mV in 0.2 M CsHCO₃, is found for the IrO₂/Ir anode, and we employed this configuration for all subsequent device work. Fig. 2f shows that the use of a more concentrated electrolyte further improves the OER activity as evidenced by an additional decrease in the overpotential, to only 300 mV in 0.5 M CsHCO₃. Multiday stability of the anode was also demonstrated as detailed in the ESI† (see IrO₂ stability measurements in ESI†).

Electrochemical energy conversion efficiency measurements

The electrochemical conversion efficiency was evaluated by operating the cell in a two-electrode mode with a CuAg nanocoral cathode and IrO₂ nanotubes on an Ir foil as the anode. The anode and cathode chambers were separated by an anion exchange membrane (Selemion) in a sandwich-type electrochemical cell.²⁴ The energy conversion efficiency was calculated for each product (H₂, CO, CH₄, C₂H₄, C₂H₆, C₂H₅OH, C₃H₇OH, *etc.*) using their standard thermodynamic potential, their Faradaic efficiency, and the total input cell voltage (see energetic efficiency calculation in ESI† for more details); below is an example calculation for ethylene:

$$\eta_{\text{energetic, C}_2\text{H}_4} = \frac{E_{\text{C}_2\text{H}_4}^0 \text{FE}_{\text{C}_2\text{H}_4}}{V_{\text{in}}} \quad (1)$$

where $E_{\text{C}_2\text{H}_4}^0$ is the standard thermodynamic potential of ethylene, $\text{FE}_{\text{C}_2\text{H}_4}$ is the faradaic efficiency of ethylene, and V_{in} is the total cell voltage. The total energetic efficiency of an electrochemical cell is the sum of the individual energetic efficiencies of all CO₂ RR products. Hydrocarbons (HCs) and oxygenates refer to ethylene, methane, ethanol, propanol, allyl alcohol, propionaldehyde, acetaldehyde, glycolaldehyde, ethylene glycol, hydroxyacetone, acetate and formate (see Table S7, ESI† for details). It is important to stress that this measurement mode accounts for

the potential losses of each component of the electrochemical cell (overpotentials of electrodes and resistance losses) and accurately defines the overall electrochemical cell efficiency. Importantly, electrochemical cell efficiency calculations should be done in a two-electrode configuration because the voltage drop at the counter electrode is unknown in three-electrode measurements.²⁶

Both the total cell voltage (3.1–4.1 V) and the electrolyte concentration (0.1–0.5 M) were varied to assess their effect on the conversion efficiency. Fig. 3a shows that the target current density can be achieved in the tested voltage range for electrolyte concentrations of 0.1 M and above. We operated the electrochemical cell over a range of conditions to find a working window in which the cell produces an operating current density of 10 ± 5 mA cm⁻². The shaded part of the J - V curve in Fig. 3a demarcates the employed working window. Fig. 3d and e illustrate the product distributions obtained by varying the voltage and the electrolyte concentration, respectively. Notably, in this two-electrode configuration, raising the voltage and/or electrolyte concentration reduces the FE to hydrogen, thereby increasing the selectivity to hydrocarbons. We compared these results with those of oxide-derived copper and found the opposite behavior: the hydrogen FE increases with voltage as well as with electrolyte concentration, reducing the selectivity to hydrocarbons (Fig. S15b, ESI†). As a result, as shown in Fig. 3b and c, the overall energetic efficiency to the target products of this study, hydrocarbons and oxygenates, is relatively constant at nearly 20% over a wide range of applied voltages and electrolyte concentrations. Also, most of these products are C₂₊ species such as ethylene, ethanol, propanol, *etc.* (refer to Table S7, ESI† for all CO₂ RR products observed in this study). We also compared this data with OD copper at same electrolyte concentrations and again found comparatively better selectivity for HCs and oxygenates for the CuAg nanocoral cathode (Fig. S11 and S12, ESI†). Minimizing the overall cell voltage while maintaining overall efficiency is essential for operating the system as a whole. We evaluated the cell performance at low voltage by operating the cell at 2.5 V in 0.5 M CsHCO₃ (below 2.5 V, hydrogen generation dominates), shown in Fig. S17 (ESI†). These conditions correspond to low light illumination in the coupled system as discussed below. A total energetic efficiency of 50.3% (Table S9, ESI†) and an energetic efficiency for hydrocarbons and oxygenates of 24% were obtained.

Solar-driven CO₂ reduction efficiency measurements

The output voltage of most practical photovoltaic (PV) cells is significantly lower than the voltage required the electrochemical cell. Current-matched PV cells can be connected in series to increase the overall voltage,¹¹ but such a configuration would have a time-varying voltage outside the operational window under variable illumination, which would affect selectivity. Instead, in this study, to achieve a potential in the window required for the electrochemical cell operation, and to maintain those conditions under variable illumination levels, we employed maximum power point (MPP) tracking circuits with boost converters as represented in Fig. 4a (see Methods for further details). Such MPP circuits can step up an initial voltage below 1 V into the

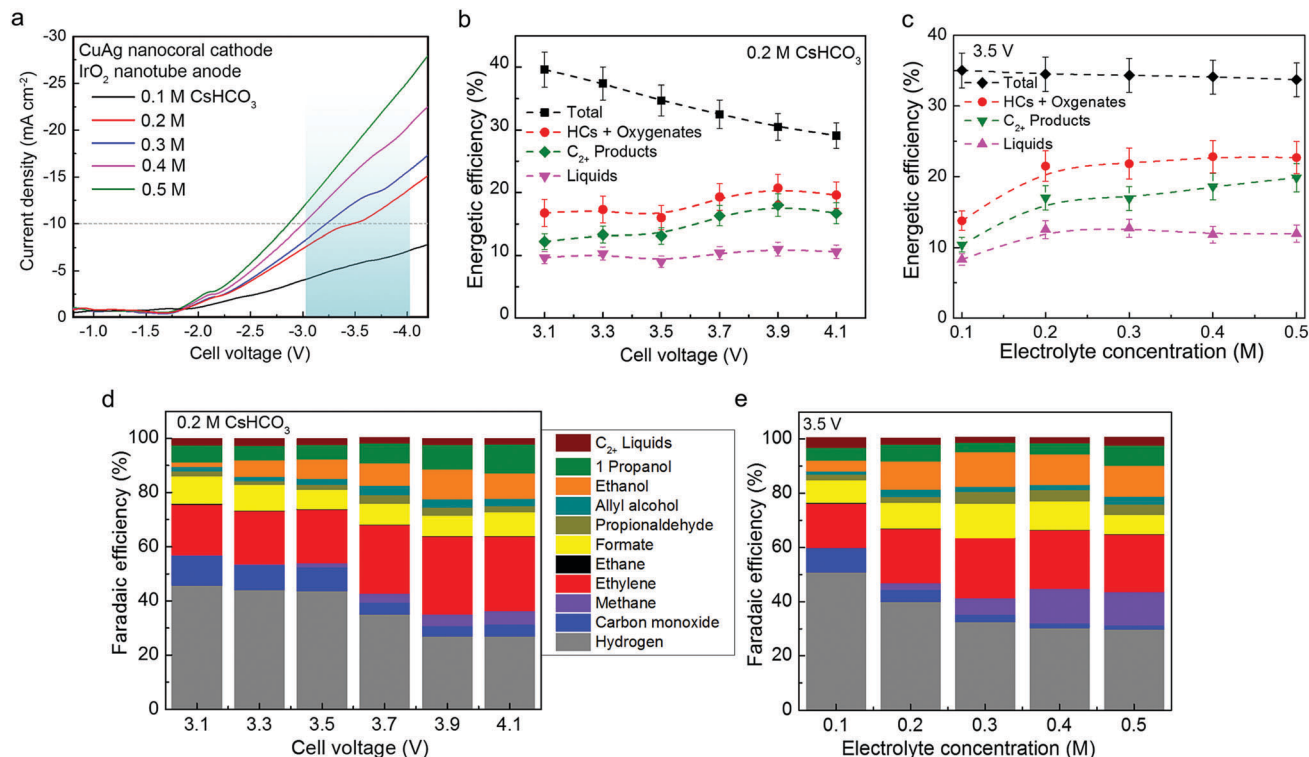


Fig. 3 CO₂ reduction performed in a two-electrode configuration with a CuAg nanocoral cathode and an IrO₂ nanotube anode. (a) Linear scan voltammetry curve of a CuAg nanocoral cathode in a two-electrode configuration with an IrO₂ nanotube anode in different electrolyte concentrations (0.1–0.5 M CsHCO₃) during CO₂ RR. The determined working window is depicted by blue shading. (b) Energetic efficiency (overall electrochemical cell conversion efficiency) as a function of applied voltage in 0.2 M CsHCO₃. (c) Energetic efficiency as a function of electrolyte concentration at a fixed applied voltage of 3.5 V. (d) CO₂ RR product distribution as a function of applied voltage in 0.2 M CsHCO₃. (e) CO₂ RR product distribution as a function of electrolyte concentration (0.1–0.5 M CsHCO₃) at a fixed applied voltage of 3.5 V.

required range with efficiencies of 90% and above. Details of the PV cells, MPP tracking circuits, and electrical configuration are in the “Solar-Driven CO₂ Data” section of the ESI†

As shown schematically in Fig. 2a, two commercially-available silicon solar cells were used to form a complete solar-to-hydrocarbon system (TD1). A second configuration was assembled utilizing two laboratory-fabricated high-efficiency III–V/silicon tandem cells connected in series to two maximum power point (MPP) trackers, which were in turn connected in parallel (TD2).²⁷ The total illumination areas of the solar cells were set based on power matching to the electrochemical cell: 3.198 cm² and 2.0 cm² for TD1 and TD2, respectively. In the case of TD1, the illuminated area was chosen to be sufficiently large to drive the EC cell even at low illumination conditions (0.35 Sun). A detailed characterization of the solar elements of TD1 and TD2 is in the ESI† At 1 Sun, the two series-connected Si cells provide an open circuit voltage (V_{oc}) of 1.1 V and a short circuit current (I_{sc}) of 61.3 mA. For TD2 at 1 Sun, the top III–V cells provide a V_{oc} of 1.44 V and 1.46 V, and an I_{sc} of 33.4 mA and 30.4 mA; the bottom silicon solar cells provide a V_{oc} of 0.7 V each and an I_{sc} of 49.8 mA and 49.4 mA (Fig. S20, ESI†).

The solar-to-chemical (STC) conversion efficiency and device stability of TD1 was measured as a function of illumination intensity (0.35 to 1.0 Sun) and electrolyte concentration (0.1–0.5 M CsHCO₃). Under these conditions, the MPP output voltage (which

is the electrochemical cell input) was in the range of 2.5–3.6 V with corresponding current densities in the range of 4.95–15.11 mA cm⁻² (see ESI† for details on each experiment, Table S8) (Fig. 4b). The current increases with electrolyte concentration due to higher ionic conductivity. Notably, the system yields a consistent product distribution over this range of conditions, as could be anticipated from the two-electrode EC measurements discussed above. The faradaic efficiency of hydrogen decreases with the electrolyte concentration, whereas that of methane increases, which is similar to our previous observation (Fig. S21, ESI†). Ethylene, ethanol and propanol are the major hydrocarbon products with a total Faradaic efficiency of 30–40% at 0.35 to 1 Sun illumination (Fig. S21, ESI†).

For the TD1 configuration, the total solar-to-chemical conversion efficiency is a maximum of 7.5% at 0.35 Sun illumination and in 0.5 M CsHCO₃ electrolyte concentration, which reduces to a minimum of 2.4% with 1 Sun and 0.1 M CsHCO₃ (Fig. S17, ESI†). The solar to hydrocarbon and oxygenate conversion efficiency is a maximum of 3.9% at 0.53 Sun illumination and 0.5 M CsHCO₃ electrolyte (Fig. 4d). Interestingly, we attained higher solar-to-chemical conversion efficiency at lower illumination because the input power decreases with illumination by a greater proportion than the current density, which is moderated by the MPP tracker (eqn (S7), ESI†). Device stability was demonstrated by a 6 h measurement of TD1 in 0.2 M CsHCO₃

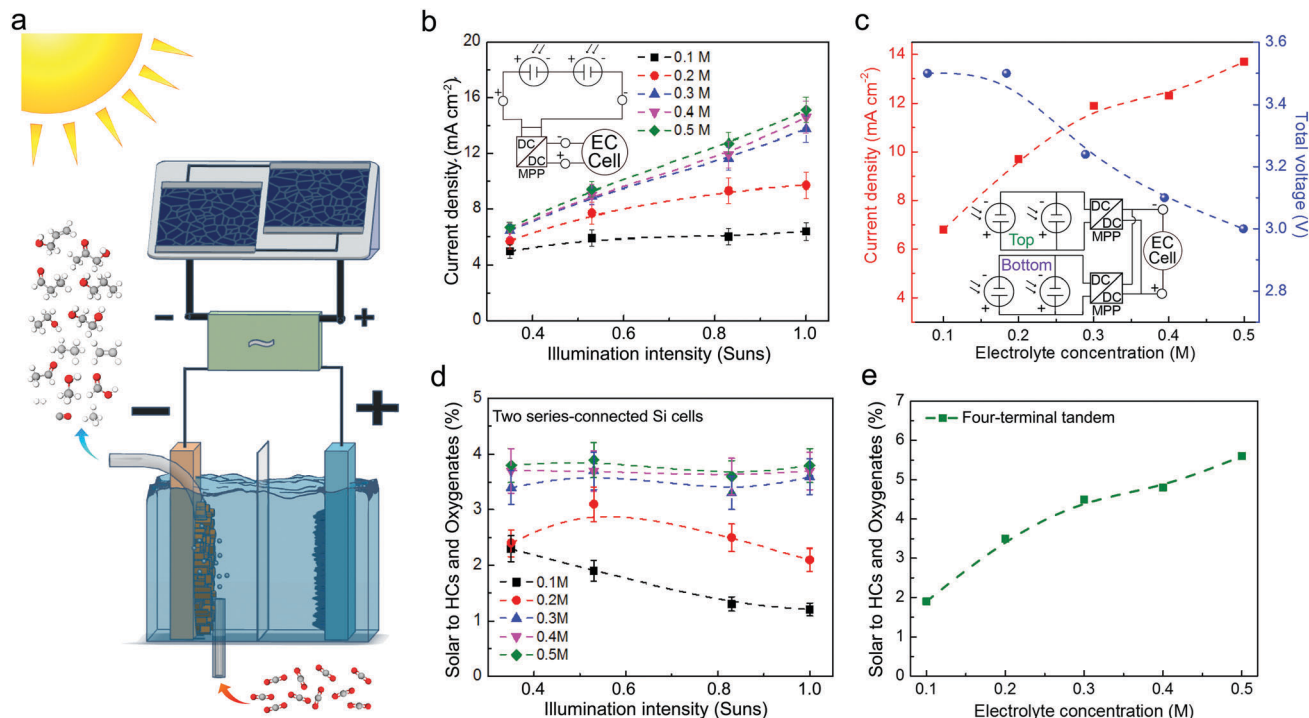


Fig. 4 Solar-driven CO₂ RR measurements performed in a two-electrode configuration with a CuAg nanocoral cathode and an IrO₂ nanotube anode in tandem with two series-connected solar cells and an MPP tracker. (a) Schematic of solar CO₂ reduction system, where larger +/- indicates voltage upconversion and thinner wires reflect reduced current. (b) Measured current density of TD1 under various electrolyte conditions as a function of illumination. (c) Measured current density (left axis, red) and voltage (right axis, blue) of TD2 as a function of electrolyte concentration at 1 Sun illumination. Inset depicts the TD2 circuit diagram. (d) Solar to hydrocarbon and oxygenate conversion efficiency of TD1 as a function of illumination. (e) Solar to hydrocarbon and oxygenate conversion efficiency of TD2 as a function of electrolyte concentration at 1 Sun illumination.

under 1 Sun illumination. As expected, the device was stable and exhibited a STC efficiency over 3.2%, and a solar to hydrocarbon and oxygenate efficiency of 2% (Fig. S23, ESI[†]). These efficiency values are in good agreement with short-term measurements, and demonstrate that the membrane is preventing product crossover to the anode.

TD2 was evaluated under 1 Sun illumination as a function of electrolyte concentration (0.1–0.5 M CsHCO₃). As the electrolyte concentration is increased, the voltage transferred to the EC cell drops from 3.5 to 3.0 V, and the current density more than doubles from 5.4 to 13.2 mA cm⁻² (Fig. 4c and Table S10, ESI[†]). Importantly, the faradaic efficiency for hydrogen decreases from 45% to 25% over this range. As a result, the system attains both its highest solar to all products (8.4%) and solar to hydrocarbon and oxygenate conversion efficiency (5.6%) at the highest electrolyte concentration, 0.5 M CsHCO₃ (Fig. 4e and Fig. S25; Table S11, ESI[†]). This conversion efficiency, as well as those obtained from TD1 over a range of illumination conditions, greatly exceeds the solar conversion efficiency of natural photosynthesis, which is estimated to be about 1%.²⁸

Experimental

Chemical and materials

All materials were used as received unless otherwise specified. Cesium carbonate (Cs₂CO₃, ACS ≥ 99.995%) was purchased

from Sigma-Aldrich. Copper foil and silver foil (0.1 mm thick, Cu and Au, each 99.999% metal basis) were purchased from Alfa Aesar. Carbon dioxide (CO₂, 99.995%), nitrogen (N₂, 99.999%), helium (He, 99.999%), and hydrogen (H₂, 99.999%) were purchased from Praxair. Electrolyte solutions were prepared with 18.2 MΩ deionized water from a Millipore system. CsHCO₃ electrolyte solutions (0.1–0.5 M) were prepared by vigorously bubbling (0.05–2.5 M) Cs₂CO₃ solutions with CO₂ gas for a few minutes to achieve the desired pH. Copper sulfate (CuSO₄, ACS ≥ 99.99% trace metal basis), zinc nitrate hexahydrate (Zn(NO₃)₂·6H₂O, Reagent Grade ≥ 98%), hexamethylenetetramine (C₆H₁₂N₄, ACS ≥ 99.0%), ethanolamine (NH₂OH, ACS ≥ 98%), 2-methoxyethanol (CH₃OCH₂CH₂OH, ≥ 99%), hydrogen peroxide solution (H₂O₂, 30 wt%), oxalic acid (C₂H₂O₄, anhydrous, ≥ 99.0%), sulfuric acid (H₂SO₄, ≥ 99.0%), and potassium carbonate (K₂CO₃, ACS ≥ 99.995%, trace metal basis) were purchased from Sigma-Aldrich. Zinc acetate (ZnC₄H₆O₄, anhydrous, ≥ 99.98%, metal basis) and iridium chloride (IrCl₄, ≥ 99.95%, metal basis) were purchased from Alfa Aesar.

Cathode preparation

Silver foil was cut into 2 cm squares and cleaned by sonication for 15 min in acetone, isopropanol, and deionized (DI) water. Silver foil electrodes were sanded with increasing grades of sandpaper from 1200 to 2500 grit and then mechanically polished with five-micron size alumina nanoparticles (TED Pella Inc., product no. 895-6-18).

The mechanically-polished silver foils were degreased in 0.1 M HCl for 5 min to remove the undesired oxide layer and finally washed in DI water for 45 min. An aqueous solution of 0.1 M copper sulfate was prepared and maintained at pH 1 by adding sulfuric acid prior to electrodeposition. The nanocoral CuAg bimetallic cathode was fabricated by a two-electrode electrodeposition method. A Teflon cell was used for electrodeposition, in which the silver foil was the working electrode and a Pt mesh was used as the counter electrode. The electrodeposition process was performed at a high constant current of 400 mA for 10 s. After electrodeposition, the CuAg cathode was washed in DI water and dried with a gentle nitrogen stream. Under high current density conditions, the competitive reaction of hydrogen evolution forms a bubble template, which defines the nanocoral morphology and also controls the amount of silver deposited at the surface.

For comparison, we synthesized an oxide-derived copper cathode following the method of Li *et al.*²⁹ Copper foil was cut into 2 cm squares and cleaned by degreasing for 30 min in acetone, isopropanol, and DI water. The electrodes were then electropolished in concentrated phosphoric acid at a potential of 2.0 V for 5 min with a copper-foil counter electrode. The electro-polished Cu foils were rinsed with DI water and dried with a stream of nitrogen. Finally, the Cu foils were annealed at 500 °C for 2 h to obtain oxide-derived copper cathodes.

IrO₂ anode preparation

We prepared high surface area IrO₂ by adapting and modifying the procedure of Zhao *et al.*²⁵ Instead of drop casting, we grew the sacrificial template with hydrothermal synthesis, which produced better uniformity. We performed hydrothermal growth of both TiO₂ and ZnO templates. However, we found that we were not able to completely remove the TiO₂ template after IrO₂ deposition whereas the ZnO nanorods could be etched easily with dilute perchloric acid. We prepared iridium foil and FTO-coated glass substrates by sonication for 15 min in acetone, isopropanol, and DI water. Iridium foil was prepared by sanding with increasing grades of sandpaper from 1200 to 2500 grit and then degreased in 0.1 M HCl for 5 min to remove the undesired oxide layer and finally rinsed in DI water for 45 min. FTO-coated glass substrates were ultrasonicated for 15 min in soap solution, decon solution, DI water, acetone, and 2-methoxyethanol. These substrates were dried with a nitrogen stream. The ZnO template was prepared by adapting a previously-reported two-step method.³⁰ First, a seed layer of ZnO was deposited by spin coating a solution of 0.1 M zinc acetate, 0.05 M ethanolamine, and 2-methoxyethanol. Two spin-coating depositions were performed: first at 500 rpm for 5 s and then at 3000 rpm for 30 s, followed by annealing at 350 °C for 5 min. This procedure was repeated three times to obtain the desired thickness of the ZnO seed layer. Finally, ZnO nanorods were grown on seed layer coated substrates *via* hydrothermal synthesis. In short, an aqueous solution of 30 mM zinc nitrate and 15 mM hexamethylenetetramine were poured into a Teflon liner with the FTO substrates and Ir foil and then heated at 95 °C for 6 h. Afterwards, the hydrothermally-grown ZnO nanorod samples were rinsed with DI water and blow dried with nitrogen.

The iridium oxide precursor solution was prepared in 4 steps: (i) 50 mL of 0.005 M iridium chloride aqueous solution (dark brown) was stirred for 30 min; (ii) 0.5 mL hydrogen peroxide (30 wt%) was added slowly and stirred for 15 min until the solution color turned from light brown to yellowish; (iii) 250 mg oxalic acid was mixed in the solution while, over 15 minutes, the solution turned to a light yellowish color; (iv) potassium carbonate was slowly added to change the pH to ~10. We aged the solution for three days until the solution turned a purple or blueish color. Electrodeposition of IrO₂ was performed in a three-electrode configuration, with FTO/Ir foil used as the working electrode, Ag/AgCl as the reference electrode, and Pt wire as the counter electrode. A cyclic voltammetry scan from 0 to 0.6 V *vs.* Ag/AgCl was repeated 30 times at a rate of 50 mV per second. After electrodeposition, the samples were soaked for 10 min in 0.01 M perchloric acid to etch the ZnO layer. Finally, the iridium oxide (IrO₂) nanotube array was washed with DI water and blow dried with nitrogen. The morphology of the IrO₂ and the absence of ZnO was confirmed with SEM and EDX measurements.

Testing of cathodes and anodes

The CO₂ RR activity of CuAg cathode was tested in a three-electrode configuration at a fixed potential of -1.0 V *vs.* RHE in 0.2 M CsHCO₃ electrolyte (pH = 7.1) in a sandwich-type polyether ether ketone (PEEK) cell purged with CO₂ at 5 sccm. IrO₂ and Ag/AgCl were used as counter and reference electrodes, respectively. The -1.0 V *vs.* RHE potential was chosen based on literature values in order to optimize the C₂₊ product selectivity.^{16,31,32}

Current-voltage measurements were carried out for IrO₂ nanotube anodes in a three-electrode configuration, with platinum foil as the counter electrode, Ag/AgCl as the reference electrode and IrO₂ nanotubes as the working electrode. The three-electrode *J-V* measurements were performed in different concentrations of CsHCO₃ electrolyte (0.1–0.5 M). Applied voltages *vs.* Ag/AgCl were converted to RHE scale using the Nernst equation. The IrO₂ nanotubes on Ir foil (Ir/IrO₂) exhibit superior performance to IrO₂ nanotubes on Ti foil (Ti/IrO₂) and to IrO₂ nanotubes on a FTO substrate.

Electrochemical cell and measurement of gas and liquid products

The compression cell and product measurement protocol used in this work have been described in detail previously;²⁴ therefore, a summary will be given here. We cleaned the sandwich cell in aqua regia or nitric acid and DI water before every measurement and each measurement was repeated several times. All the gaseous products were measured with an inline GC (SRI 8610C) and liquid samples were collected after GC measurements and fed to the high-performance liquid chromatograph (HPLC) for liquid products analysis.

Power matching electronics

Coupling of two Si PV cells in series to the electrochemical cell was accomplished with an MPP tracker (Texas Instruments BQ25504EVM-674 board with integrated inductive boost converter) which, as received, can supply voltages up to 2.9 V from a minimum

0.9 V input. The output voltage was adjusted to suit our target voltage range by replacing the fixed feedback resistor (5.9 M Ω) on the board with an adjustable potentiometer (3–7 M Ω).

The four terminal III–V/Si tandem solar cells were interfaced to two modified MPP trackers. One MPP tracker was connected with two outer (top) series-connected III–V absorbers, while other MPP tracker was connected to the two bottom Si absorbers. These two MPP circuits were connected in parallel to each other and to the electrochemical cell to provide constant voltage. We used two MPP trackers to avoid spectrum mismatch between the top and bottom absorbers (see solar to hydrocarbons discussion in the ESI† for details).

Solar-driven CO₂ reduction cell

Solar-driven measurements of TD1 and TD2 were conducted by a calibrated xenon lamp equipped with AM 1.5G and AM0 filters. Optical neutral density filters were used to control the illumination intensities (see solar to hydrocarbons in ESI† for details). A pyranometer (SolarLight Co. Inc., Model: PMA2144) was used to calibrate the power density for different optical density filter configurations. A certified silicon solar cell (Newport, Model: 91150V) was used to calibrate the light intensity. CO₂ was purged continuously at a rate of 5 sccm during the measurement.

Conclusions

The large overpotential requirements for electrochemical CO₂ reduction into multi-electron products had limited the overall conversion efficiency of EC and PV–EC devices. Here, we have critically evaluated all components of the EC cell to minimize the voltage losses while maintaining selectivity. An electrodeposited CuAg nanocoral cathode is shown to exhibit superior selectivity (~70%) to C₁–C₃ products over a wide potential and electrolyte concentration range. A highly-active IrO₂ nanotube anode is used to reduce the overpotential required for water oxidation. Use of MPP tracker electronics is used to keep the PV-connected EC cell within its operational window over a range of illumination conditions. Two series-connected silicon solar cells, an MPP tracker, and an electrochemical cell in combination result in a stabilized power output and reduce CO₂ into hydrocarbons and oxygenates with a maximum conversion efficiency of 3.9%, while a four-terminal tandem cell assisted device achieved a peak solar to hydrocarbon and oxygenate conversion efficiency of 5.6%. Both conversion efficiencies far exceed that for natural photosynthesis. The modular nature of the approach we employed will allow for further improvements in efficiency, particularly if a cathode which can selectively produce hydrocarbons and oxygenates at lower overpotentials can be discovered.

Conflicts of interest

There are no conflicts to declare.

Acknowledgements

We thank Jeffrey Beeman for technical assistance with the power-matching electronics and James Wu for providing high purity Ir foils. This material is based on the work supported by the Joint Center for Artificial Photosynthesis (JCAP), a DOE Energy Innovation Hub, supported through the Office of Science of the U.S. Department of Energy under Award Number DE-SC0004993. The PV device selection and testing and the design and assembly of the power matching electronics was supported by the Bay Area Photovoltaic Consortium under Award Number DE-EE0004946. Transmission electron microscopy was performed at the Molecular Foundry, Lawrence Berkeley National Laboratory, and was supported by the Office of Science, Office of Basic Energy Sciences, of the U.S. Department of Energy under Contract No. DE-AC02-05CH11231. We thank Stephanie Essig and Adele Tamboli for providing the III–V/Si tandem solar cell, which was developed as part of a collaboration between the National Renewable Energy Laboratory (NREL), Swiss Center for Electronics and Microtechnology (CSEM) and École polytechnique fédérale de Lausanne (EPFL). DS acknowledges fellowship support from the Hungarian American Enterprise Scholarship Fund (HAESF CIEE) and the National Research, Development and Innovation Office (NKFIH PD 121318). YL acknowledges the support of an A*STAR National Science Scholarship.

References

- 1 C. Graves, S. D. Ebbesen, M. Mogensen and K. S. Lackner, *Renewable Sustainable Energy Rev.*, 2011, **15**, 1–23.
- 2 S. Chu, Y. Cui and N. Liu, *Nat. Mater.*, 2016, **16**, 16–22.
- 3 J. Rongé, T. Bosserez, D. Martel, C. Nervi, L. Boarino, F. Taulelle, G. Decher, S. Bordiga and J. A. Martens, *Chem. Soc. Rev.*, 2014, **43**, 7963–7981.
- 4 J. H. Montoya, L. C. Seitz, P. Chakhranont, A. Vojvodic, T. F. Jaramillo and J. K. Nørskov, *Nat. Mater.*, 2016, **16**, 70–81.
- 5 J. W. Ager, M. R. Shaner, K. A. Walczak, I. D. Sharp and S. Ardo, *Energy Environ. Sci.*, 2015, **8**, 2811–2824.
- 6 M. A. Modestino and S. Haussener, *Annu. Rev. Chem. Biomol. Eng.*, 2015, **6**, 13–34.
- 7 M. Schreier, L. Curvat, F. Giordano, L. Steier, A. Abate, S. M. Zakeeruddin, J. Luo, M. T. Mayer and M. Grätzel, *Nat. Commun.*, 2015, **6**, 7326.
- 8 T. Arai, S. Sato and T. Morikawa, *Energy Environ. Sci.*, 2015, **8**, 1998–2002.
- 9 X. Zhou, R. Liu, K. Sun, Y. Chen, E. Verlage, S. A. Francis, N. S. Lewis and C. Xiang, *ACS Energy Lett.*, 2016, **1**, 764–770.
- 10 T. Arai, S. Tajima, S. Sato, K. Uemura, T. Morikawa and T. Kajino, *Chem. Commun.*, 2011, **47**, 12664.
- 11 M. Schreier, L. Curvat, F. Giordano, L. Steier, A. Abate, S. M. Zakeeruddin, J. Luo, M. T. Mayer and M. Grätzel, *Nat. Commun.*, 2015, **6**, 7326.
- 12 M. Schreier, F. Horéguel, L. Steier, S. Ahmad, J. S. Luterbacher, M. T. Mayer, J. Luo and M. Grätzel, *Nat. Energy*, 2017, **2**, 17087.

- 13 J. L. Young, M. A. Steiner, H. Döscher, R. M. France, J. A. Turner and T. G. Deutsch, *Nat. Energy*, 2017, **2**, 17028.
- 14 S. A. Bonke, M. Wiechen, D. R. MacFarlane and L. Spiccia, *Energy Environ. Sci.*, 2015, **8**, 2791–2796.
- 15 C. W. Li and M. W. Kanan, *J. Am. Chem. Soc.*, 2012, **134**, 7231–7234.
- 16 Y. Hori, A. Murata and R. Takahashi, *J. Chem. Soc., Faraday Trans. 1*, 1989, **85**, 2309.
- 17 Y. Hori, in *Modern Aspects of Electrochemistry*, ed. C. G. Vayenas, R. E. White and M. E. Gamboa-Aldeco, Springer, New York, New York, NY, 2008, pp. 89–189.
- 18 X. Feng, K. Jiang, S. Fan and M. W. Kanan, *J. Am. Chem. Soc.*, 2015, **137**, 4606–4609.
- 19 J. J. L. Humphrey, D. Plana, V. Celorrio, S. Sadasivan, R. P. Tooze, P. Rodríguez and D. J. Fermín, *ChemCatChem*, 2016, **8**, 952–960.
- 20 A. Murata and Y. Hori, *Bull. Chem. Soc. Jpn.*, 1991, **64**, 123–127.
- 21 M. R. Singh, Y. Kwon, Y. Lum, J. W. Ager and A. T. Bell, *J. Am. Chem. Soc.*, 2016, **138**, 13006–13012.
- 22 Y. Lum, B. Yue, P. Lobaccaro, A. T. Bell and J. W. Ager, *J. Phys. Chem. C*, 2017, **121**, 14191–14203.
- 23 M. R. Singh, E. L. Clark and A. T. Bell, *Phys. Chem. Chem. Phys.*, 2015, **17**, 18924–18936.
- 24 P. Lobaccaro, M. R. Singh, E. L. Clark, Y. Kwon, A. T. Bell and J. W. Ager, *Phys. Chem. Chem. Phys.*, 2016, **18**, 26777–26785.
- 25 C. Zhao, H. Yu, Y. Li, X. Li, L. Ding and L. Fan, *J. Electroanal. Chem.*, 2013, **688**, 269–274.
- 26 D. T. Whipple and P. J. A. Kenis, *J. Phys. Chem. Lett.*, 2010, **1**, 3451–3458.
- 27 S. Essig, M. A. Steiner, C. Allebe, J. F. Geisz, B. Paviet-Salomon, S. Ward, A. Descoeurdes, V. LaSalvia, L. Barraud, N. Badel, A. Faes, J. Levrat, M. Despeisse, C. Ballif, P. Stradins and D. L. Young, *IEEE J. Photovoltaics*, 2016, **6**, 1012–1019.
- 28 R. E. Blankenship, D. M. Tiede, J. Barber, G. W. Brudvig, G. Fleming, M. Ghirardi, M. R. Gunner, W. Junge, D. M. Kramer, A. Melis, T. A. Moore, C. C. Moser, D. G. Nocera, A. J. Nozik, D. R. Ort, W. W. Parson, R. C. Prince and R. T. Sayre, *Science*, 2011, **332**, 805–809.
- 29 C. W. Li, J. Ciston and M. W. Kanan, *Nature*, 2014, **508**, 504–507.
- 30 Y. F. Hsu, Y. Y. Xi, A. B. Djurišić and W. K. Chan, *Appl. Phys. Lett.*, 2008, **92**, 133507.
- 31 A. S. Varela, M. Kroschel, T. Reier and P. Strasser, *Catal. Today*, 2016, **260**, 8–13.
- 32 S. Rasul, D. H. Anjum, A. Jedidi, Y. Minenkov, L. Cavallo and K. Takanabe, *Angew. Chem., Int. Ed.*, 2015, **54**, 2146–2150.